communications chemistry

Article

https://doi.org/10.1038/s42004-024-01366-1

A van der Waals porous crystal featuring conformational flexibility and permanent porosity for ultrafast water release

Kentaro Maejima[1], Heishun Zen[2], Hiroyasu Sato[3], Eiji Nishibori[4], Tomoya Enjou[5], Youhei Takeda[5], Satoshi Minakata[5], Eri Hisamura[6], Ken Albrecht[6], Yuka Ikemoto[7], Irene Badía-Domínguez[8], Juan Sánchez-Rincón[8], M. Carmen Ruiz Delgado[8], Yohei Yamamoto[1,9] ✉ & Hiroshi Yamagishi[1,9] ✉

Flexibility has been pursued enthusiastically in the field of porous crystals for enhancing their adsorption and separation performances. However, flexibility has never been observed among porous crystals sustained thoroughly by van der Waals interactions since flexible motions readily lead to the collapse of the porous architecture. Here we report a van der Waals crystal featuring conformational flexibility as well as permanent microporosity. The single-crystal structure and its structural transition in response to the adsorption of water molecules were unambiguously disclosed by means of electron and X-ray crystal structure analyses. The peripheral aromatic rings of the constituent molecule rotated as increasing the ambient humidity, while the connectivity of the pores was maintained throughout the structural transition. The transformative pores allowed the guest water molecules to move exceedingly quickly through the pores with a time constant of 490 μs. We demonstrated that the quick release of water induced by photothermal heating induced a significant upward bending of a film set above the crystalline powder compared to conventional porous materials. This finding contributes to the future crystal engineering based on van der Waals interactions rather than cohesive bonds.

Historically, porous crystals with structural flexibility have been a challenging target to synthesize because the flexible molecules transform and translocate readily in the crystal to fill the pores[1–5]. In the early 2000's, researchers found that flexible porous crystals can be synthesized by introducing a intermolecular bonding network together with flexible linkers and deformable nodes[6–9]. The intermolecular bonding network with sufficient bonding strength makes the porous framework robust and tolerant against the evacuation of the guest molecules, as exemplified by metal-organic, covalent organic and hydrogen-bonded frameworks (MOFs, COFs and HOFs), while the flexible components enable the transformation of the lattice in response to the uptake or release of guest molecules[10,11]. Even when the transformation is significant, the original porous structure can be retrieved just by exposing the polymorph to an appropriate vapor because the bonding network ensures that the constituent molecules hold their arrangement and connectivity in the guest-free state and prevents from collapsing into a polymorph with a totally distinct packing regime.

Porous van der Waals crystals are one of the most fragile classes of porous materials sustained thoroughly by van der Waals contacts and have been beyond the scope of crystal engineering because the conventional bonding network strategy based on strong intermolecular interactions is unapplicable[3,5]. Typically, a van der Waals porous crystal holds its porous framework merely by interdigitation and steric fitting that freezes the conformational and translocational motions of the constituent molecules and prevents the porous architecture from collapsing. Such delicate and intricate molecular packing is hardly designable in general, even with the latest crystal engineering technique, leading to the very small number of compounds known so far[12–20]. Incorporating flexibility into van der Waals porous crystals, namely, the synthesis of van der Waals crystals with flexible

---

[1]Department of Materials Science, Institute of Pure and Applied Sciences, University of Tsukuba, 1-1-1 Tennodai, Tsukuba, Ibaraki, 305-8573, Japan. [2]Institute of Advanced Energy, Kyoto University, Gokasho, Uji, Kyoto, 611-0011, Japan. [3]Rigaku Corporation, 12-9-3 Matsubara, Akishima, Tokyo, 196-8666, Japan. [4]Department of Physics, Institute of Pure and Applied Sciences, University of Tsukuba, 1-1-1 Tennodai, Tsukuba, Ibaraki, 305-8573, Japan. [5]Department of Applied Chemistry, Graduate School of Engineering, Osaka University, 2-1 Yamadaoka, Suita, Osaka, 565-0871, Japan. [6]Institute for Materials Chemistry and Engineering, Kyushu University, 6-1 Kasuga-Koen, Kasuga-shi, Fukuoka, 816-8580, Japan. [7]Japan Synchrotron Radiation Research Institute (JASRI) SPring-8, 1-1-1 Koto, Sayo, Hyogo, 679-5198, Japan. [8]Department of Physical Chemistry, University of Malaga, Campus de Teatinos s/n, 29071 Malaga, Spain. [9]These authors jointly supervised this work: Yohei Yamamoto, Hiroshi Yamagishi. ✉e-mail: yamamoto@ims.tsukuba.ac.jp; yamagishi.hiroshi.ff@u.tsukuba.ac.jp

and permanent pores, is an even more formidable challenge and has never been achieved so far. Actually, it is well-known that even a slight change in the conformation results in the transition into a non-porous polymorph[12,21], which never turns back into the original porous structure unless it is recrystallized from a solution state or fueled with an appropriate stimulus.

Here we report a van der Waals porous crystal featuring conformational flexibility as well as the permanent porosity (Fig. 1a, b). The van der Waals porous crystal (**VPC-1**) was assembled from a fully aromatic dendrimer **G2DBPHZ** consisting of a dibenzo[*a,j*]phenazine (DBPHZ) core and a pair of second-generation carbazole (Cz) dendrons (Fig. 1c)[22]. Electron diffraction structure analysis disclosed the single-crystal structure of **VPC-1** unambiguously, in which DBPHZ core stacked on one another thoroughly via van der Waals forces to form one-dimensional pores and Cz dendrons were exposed to the pores. X-ray structure analysis revealed the flexible motion of the Cz dendrons in response to the ambient humidity, while the DBPHZ core maintained its one-dimensional columnar arrangement throughout the transition. We also found that the conformational change, together with the fully aromatic surface of the pores, facilitated the transportation of the water molecules through the pores. Time-dependent change in diffuse reflectance upon photoexcitation with an infrared (IR) laser pulse revealed the ultrafast sorption kinetics of water in **VPC-1** with a desorption time constant of 490 μs, which is the fastest among the reported porous crystals. As a demonstration of the fast water sorption kinetics, we set a cellophane film above a stack of powdery **VPC-1** and shined a visible light onto the powder so that the crystals were heated photothermally and emitted water vapor. The humidification with **VPC-1** was so quick and intense that the film bent upward more significantly than those induced by other authentic porous materials.

Results and discussion

Crystal structure analysis of VPC-1

G2DBPHZ was synthesized according to our previous report[22] and was crystalized to yield **VPC-1** by diffusing MeOH vapour into a $CHCl_3$ solution of **G2DBPHZ** in a sealed glass vial standing at 25 °C in 17 days (Fig. S1). The powdery specimen of **VPC-1** appeared single-crystalline in microscopic images, although the grain size was not enough for X-ray single-crystal structure analysis (Fig. S2). Alternatively, we conducted electron diffraction for the crystal structure analysis by using Rigaku XtaLAB Synergy-ED (MicroED) and succeeded in solving the single-crystal structure (Fig. 1, Table S1, and Supplementary Data 1).

The crystal belonged to the polar space group of *Cm* and is solely composed of **G2DBPHZ** without any guests since the analysis was performed under vacuum in the MicroED (Fig. 1a). **G2DBPHZ** packed one-dimensionally via π–π interactions in such a way that the central DBPHZ core and the peripheral Cz rings respectively stacked on their own. The π–π stacking was perfectly linear along the *a* axis without any displacement along the *b* axis and without any rotational displacement. The columns are packed in parallel with each other in the crystallographic *bc* plane, forming two types of extrinsic pores. The atomic contacts found between the columns were only H···H, meaning that **VPC-1** is a pure van der Waals molecular crystal. The weak intermolecular interactions between the columns are highly beneficial for allowing **G2DBPHZ** to transform smoothly in response to moderate chemical or physical stimuli. The perfectly linear π–π stacking is generally static and will not be destroyed easily, which is advantageous for preserving the molecular arrangement throughout the flexible motion. Density functional theory (DFT) calculations for dimers extracted from the crystal structures along the different directions support that the intercolumnar interactions are very weak compared to π-π interactions (Fig. S3).

The structural transition of **VPC-1** in response to the change in humidity was analyzed based on powder X-ray diffraction (PXRD). We filled two glass capillaries (diameter of 0.7 mm) with fine powder of **VPC-1** and sealed them under 0 and 92%RH, respectively. The capillaries were subjected to the irradiation of synchrotron X-ray ($\lambda = 1.0$ Å), and the diffraction profiles were analyzed using the Rietveld refinement method, revealing the crystal structures of **VPC-1** including H_2O, although the location of H_2O is partially uncertain. The packing diagram under 0%RH was nearly the same as that under vacuum but incorporated a small amount of water molecules in the pores (Fig. S4, Table S2, and Supplementary Data 2), which was plausibly the residual water remaining in the specimen due to the incomplete drying. The packing diagram under 92%RH was basically analogous to that under 0%RH except that the pores were fully occupied with water molecules (Fig. 1b, Table S2, and Supplementary Data 3). Concomitant with the pore filling, **G2DBPHZ** showed some

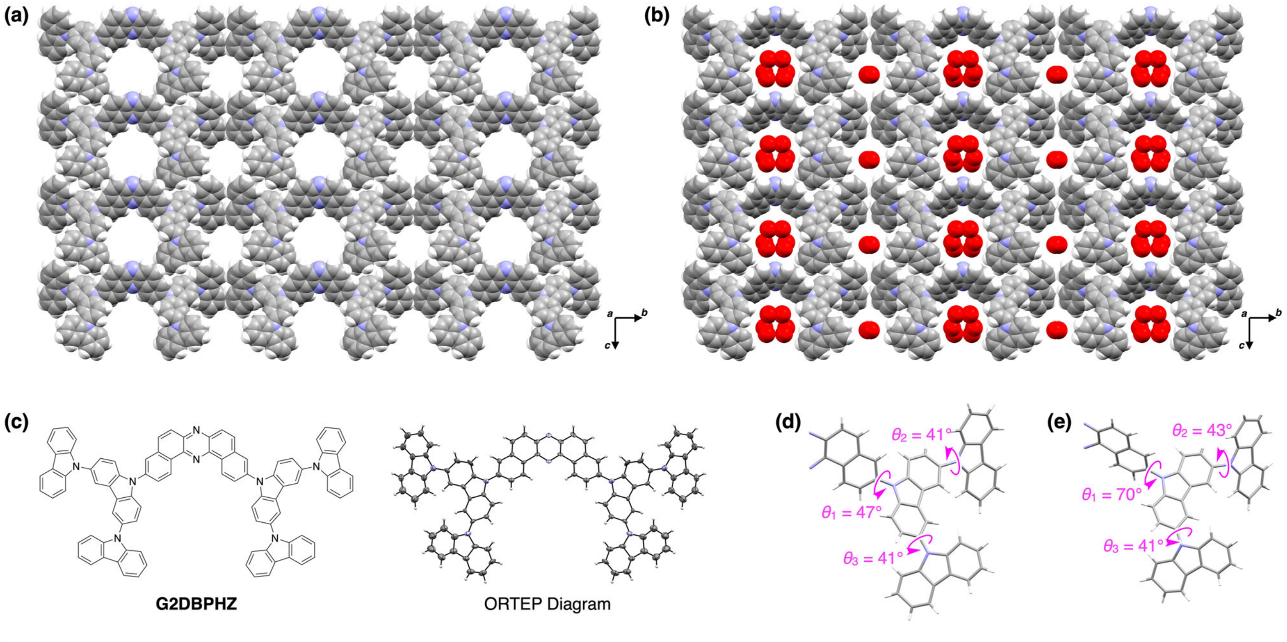

Fig. 1 | Crystal structures of VPC-1. a, **b** Crystal packing diagram of **VPC-1** under vacuum (**a**) and under atmosphere with a humidity of 92%RH (**b**). The red spheres represent the oxygen atoms of water molecules adsorbed in **VPC-1**. **c** Molecular structure of **G2DBPHZ** and the corresponding ORTEP representation observed in the single-crystal structure. **d**, **e** Dihedral angles between the DBPHZ core and internal Cz unit (θ_1), and between the internal and external Cz units (θ_2 and θ_3) observed under vacuum (**d**) and under an atmosphere with a humidity of 92% RH (**e**).

conformational changes. The internal Cz units rotated by 23° around the single bonds, and the two external Cz units rotated by 2° in comparison to those observed in vacuum (Fig. 1d, e). These results were consistent with the vibrational spectroscopic data observed experimentally and computationally. We previously reported that the Raman scattering and IR absorption spectra showed slight spectral changes as a function of humidity (Fig. S5)[22]. In addition to these reported experiments, we have now built molecular models based on the newly observed crystallographic structures and found that the rotation of the Cz units reproduced the IR spectral changes well (Fig. S6). In particular, the computational simulation showed good agreement with experiments regarding the spectral changes of the IR vibrational bands at around 1370 cm^{-1}, assigned to the stretching mode of the C–N bond between the inner Cz and the DBPHZ unit and the C–H bending of the central core (Fig. S6), which is an indicator of the rotation of the Cz unit with respect to the DBPHZ. The conformational flexibility of the Cz dendrons with respect to the central DBPHZ core has been explored computationally. Interestingly, a rather flat torsional potential has been found, with a small energy difference of 3.3 kcal/mol between the perpendicular conformation and the most stable conformer with a dihedral angle of ~50° (Fig. S7). This explains the facility of the outer arms of the Cz to rotate and accommodate in such a way as to maximize π-π interactions, adjusting the transformation of the crystal structure after adsorption (Fig. S8–S11).

The N_2 and H_2O adsorption isotherms of **VPC-1** were reported previously and were reproduced in the supplementary information as Fig. S12 (Supplementary Data 4–7). The abrupt increase in N_2 uptake at lower relative pressure (P/P_0) region indicates the microporosity of **VPC-1**, which is consistent with the single-crystal structure shown in Fig. 1a. The adsorption of H_2O in **VPC-1** happens abruptly at $P/P_0 = 0.5$, although the cause of the abrupt increase was not evident in the previous paper. Judging from the crystal structures revealed herein, we presume that the sudden uptake of H_2O and the structural change of **VPC-1** happen simultaneously. The transformation of the porous framework may allow the H_2O molecules to form clusters with optimum geometry and thereby suddenly accelerate the uptake of H_2O. The hydrogen bonds between guest H_2O molecules and the nitrogen atoms of DBPHZ that are exposed to the pore may be also influential to the structural transition, while it is not conclusive due to the uncertainty of the location of H_2O. DFT-optimized geometries of a **G2DBPHZ** dimer with one and two H_2O molecules support the formation of hydrogen bonds between the H_2O molecules and with the N atoms of the DBPHZ core (Fig. S13). The binding energies of the H_2O molecules are-doubled by the presence of the second H_2O molecule; however, our results show that π−π stacking interactions have a higher contribution to aggregation than the hydrogen bonding to water (i.e., compare Figs. S13 and S8).

The pore volume of **VPC-1** calculated based on the single-crystal structure was 737 $Å^3$ per unit cell ($V = 3646.39$ $Å^3$) for N_2 and 780 $Å^3$ for H_2O. The fractional filling for N_2 at $P/P_0 = 0.96$ and 77 K is 26%, and the fractional filling for H_2O at $P/P_0 = 0.92$ at 293 K is 36%. The relatively low pore filling is attributed to the one-dimensional pores of **VPC-1**, which are often stuck and become inaccessible with the gas. The isotherms of Fig. S12b–d were conducted with the same specimens, indicating the intactness of the H_2O adsorption performance of **VPC-1** even upon repeating the H_2O adsorption and desorption. The PXRD profiles also revealed the structural stability of **VPC-1** against H_2O. The PXRD profiles of **VPC-1** showed negligible change even after 10 cycles of H_2O adsorption and desorption (Fig. S14).

H_2O sorption kinetics in VPC-1

Sorption kinetics is one of the key figures of merit for porous crystals since the diffusivity as well as sorption selectivity dominates the separation efficiency[23] and charging/discharging rates of guests. In contrast to most MOFs, COFs, and HOFs that are harnessed with hydrophilic units such as metal ions, ester or imide bonds, and hydrogen bond acceptors and donors, **VPC-1** is distinct in that it is purely composed of van der Waals contacts, and its pore surface is covered fully with aromatic rings. Considering the general understanding that weaker adhesion to the pore surface accelerates the diffusion of the guest molecules in the pores[24], we presumed that the pores in **VPC-1** are less affinitive to H_2O and can accelerate the transportation of H_2O in the pores. The conformational change of **G2DBPHZ** associated with the H_2O sorption is also beneficial for enhancing the sorption kinetics because the structural transition often makes the sorption profile discontinuous in analogy to phase transition[10,25].

We investigated the sorption kinetics using a specific surface area & pore size analyzer and found that **VPC-1** showed a drastic drop in the pressure just after introducing the H_2O vapor, which is distinct from those of conventional porous materials including two types of activated carbons, carbon nanotubes, and zeolite (Fig. S15). The half decay period of the H_2O pressure observed for **VPC-1**, two types of activated carbons, carbon nanotubes, and zeolite were 1.5, 9.6, 21.0, 7.7 and 14.0 sec (Supplementary Data 6 and 8–11). The faster H_2O sorption kinetics of **VPC-1** was appreciable, but we thought that the rate could be much faster judging from the fact that the rapid decay in Fig. S15 at the initial stage was close to the minimum time-resolution observable with the specific surface area & pore size analyzer. For further elucidating the water desorption rate in a shorter time region, we built up a setup by combining a diffuse reflectance photometer and a free electron laser (FEL, pulse width of 3 μs and a repetition rate of 2 Hz)[26] generating short pulses of IR laser (Fig. S16). The short and intense IR pulse excited **VPC-1** thermally and led to the release of water within a very short period. The release of water from **VPC-1** was quantified based on the change in diffuse reflectance at 532 nm, which was made possible thanks to the hydrochromic behavior of **VPC-1** from red to yellow upon decreasing the humidity. The details of the hydrochromic behavior of **VPC-1** were reported previously[22]. The powder specimen of **VPC-1** was set in a steel chamber, where the ambient humidity was regulated with a precision of less than 1%RH. We confirmed the accuracy of the diffuse reflectance

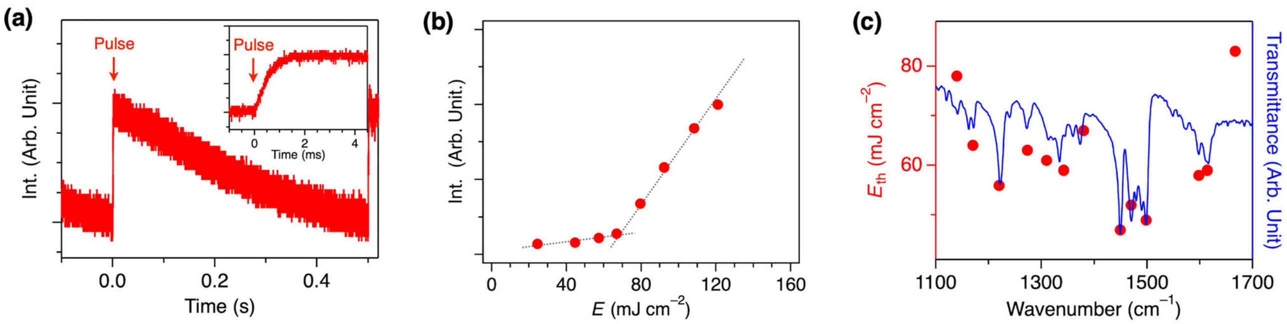

Fig. 2 | H_2O desorption from VPC-1 upon irradiation of IR pulses. a Time-course change in diffuse reflectance of **VPC-1** at 532 nm. The IR pulse (1449 cm^{-1}) was cast at $t = 0$ s with a repetition rate of 2 Hz. Inset shows the magnified image at $t = 0$ s. **b** Plot of the diffuse reflectance as a function of energy density (E) of the incident IR pulse (1380 cm^{-1}). Dotted lines are eye guides, and their crossing point indicates the threshold E (E_{th}) for the H_2O desorption. **c** Plot of E_{th} as a function of the wavenumber of the incident IR pulse (red circles) and transmittance spectrum of **VPC-1** (blue curve).

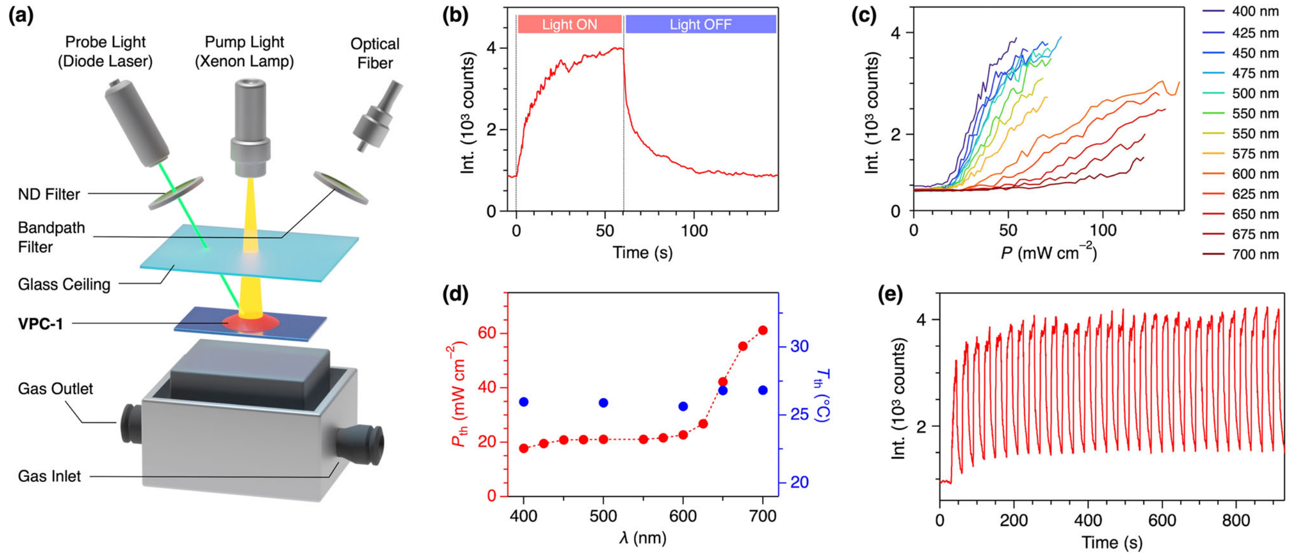

Fig. 3 | H_2O desorption from VPC-1 upon irradiation of visible light. **a** Experimental setup for measuring moisture release from **VPC-1** based on the diffuse reflectance. **b** Time-course change in diffuse reflectance of **VPC-1**. The pump light ($\lambda = 500$ nm) with a power density (P) of 80.2 mW cm^{-2} was turned on at $t = 0$ s and was turned off at $t = 60$ s. **c** Diffuse reflectance of **VPC-1** as a function of P and λ of the pump light. **d** A plot of the threshold P (P_{th}) as a function of λ of the pump light (red circles), at which **VPC-1** started to desorb H_2O. Together with the plot of P_{th}, the temperature of **VPC-1** at P_{th} (T_{th}) is also plotted (blue circles). **e** Time-course changes in diffuse reflectance of **VPC-1** when turning on the pump light for 15 s and off the light for 15 s repeatedly.

as an indicator of the water content in **VPC-1** by observing the diffuse reflectance upon incrementing and decrementing the ambient humidity from 0.6 to 82.7%RH (Fig. S17).

Using the setup, we confirmed that the incident IR pulses actually induced the release of water from **VPC-1**, and the release was detectable based on the change in diffuse reflectance as designed. Just after the incidence of the IR pulse (1449 cm^{-1}) at 50.2%RH, the diffuse reflectance at 532 nm showed a prompt increase (Fig. 2a). The rising curve of the diffuse reflectance fit well with an exponential curve with a time constant of 490 µs (Fig. 2a, inset), proving that the pulse instantaneously excited the powder, and the water molecules desorbed from **VPC-1** with a fixed time constant. In 6.0 ms after the pulse pumping, the diffuse reflectance reached a plateau and gradually decreased back to the initial value until the next pulse came (0.5 s), which is attributed to the heat dissipation from **VPC-1** to the surrounding atmosphere and to the substrate (Fig. 2a). The rate of the water desorption (490 µs) revealed herein is the fastest among the hitherto reported hydrochromic materials[27].

The change in diffuse reflectance showed a curved profile as a function of the energy density (E) of the IR pulse (Fig. 2b). When pumping with IR pulse with a wavenumber of 1380 cm^{-1}, which coincides with the absorption band of the stretching vibration of C–N single bonds and bending vibration of aromatic C–H bonds of **G2DBPHZ** (Fig. S6), the rise in diffuse reflectance became steeper when E exceeded a threshold (E_{th}) at 67 mJ cm^{-2} (Fig. 2b). Here, E_{th} is defined as the E value at the crossing point of the two regression lines obtained from the data points at lower and higher E, respectively. With an assumption that some of the bands might induce the color change more efficiently, we excited the neighboring vibrational bands with a wavenumber ranging from 1140 to 1667 cm^{-1}. Nonetheless, the observed E_{th} simply correlated with the transmittance of the bands (Fig. 2c and S18), indicating that the water release was induced by the photothermal heating of **VPC-1**. The energy of IR light was absorbed more efficiently, and the powder was heated more intensely when exciting the intense IR absorption band of **G2DBPHZ**, inducing the H_2O desorption even at smaller E. The photothermally heated **VPC-1** is then cooled by the surrounding atmosphere eventually after the IR pulse irradiation and adsorbs H_2O from the atmosphere, which is evident from the gradual recovery of diffuse reflectance (Fig. 2a).

Water vapor release from VPC-1 in response to light

We found that visible light can also induce the water release from **VPC-1** as well as IR pulses via photothermal effect. **VPC-1** was irradiated with greenish blue light ($\lambda = 487.5$–512.5 nm) as the pump light with a power density P of 80.2 mW cm^{-2} for 60 s at 23 °C and at a humidity of 63% RH (Fig. 3a). Immediately after shining the pumping light, **VPC-1** turned from red to yellow, and the diffuse reflectance at 532 nm increased by 367% (Fig. 3b). The rise in the diffuse reflectance reached a plateau in 41 s, at which 90% of the intensity change completed. The diffuse reflectance recovered back to the initial value in 75 s after stopping the pump light.

The color change of **VPC-1** was not in a linear relationship with P of the pump light but showed a curved profile with a power threshold, at which **VPC-1** started to release water (Fig. 3c). When shining a pump light with λ of 500 nm, the change in the diffuse reflectance at 532 nm was negligible when P as less than 20 mW cm^{-2}. When P was larger than 20 mW cm^{-2}, the diffuse reflectance started to increase linearly. We define the threshold power (P_{th}) as the power at the crossing point of the two regression lines obtained from the lower and higher power regions, respectively. P_{th} depended on λ of the pump light as summarized in Fig. 3d (red circles). P_{th} was nearly constant below 600 nm and became larger gradually above 600 nm, resembling the diffuse reflectance spectrum of **VPC-1** reported previously[22].

The photothermal effect was assessed by measuring the temperature of **VPC-1** during the light irradiation with a thin thermocouple probe, which was carefully set in the stack of powdery **VPC-1** so that the tip was fully covered with the powder but did not have any contact with the glass plate (Fig. S19). As increasing P of the pumping light, the temperature of **VPC-1** increased with a linear positive slope. The slope became steeper when shining an incident light with a shorter wavelength (Fig. S20). We found that the temperature at P_{th} (T_{th}) was nearly constant at 26.2 °C regardless of λ of the incident light (Fig. 3d, blue circles). Consequently, we concluded that the pump light increased the temperature of **VPC-1** via photothermal effect and induced the release of water, whose wavelength-dependent efficiency was affected by the absorption coefficient of **VPC-1**. The IR pulses at E_{th} are also supposed to increase the temperature of **VPC-1** to 26 °C.

The H_2O desorption kinetics is calculated quantitatively based on the change in temperature and adsorption isotherm in Fig. S12. The temperature of **VPC-1** increases from 22.6 to 35.0 °C upon irradiation of laser

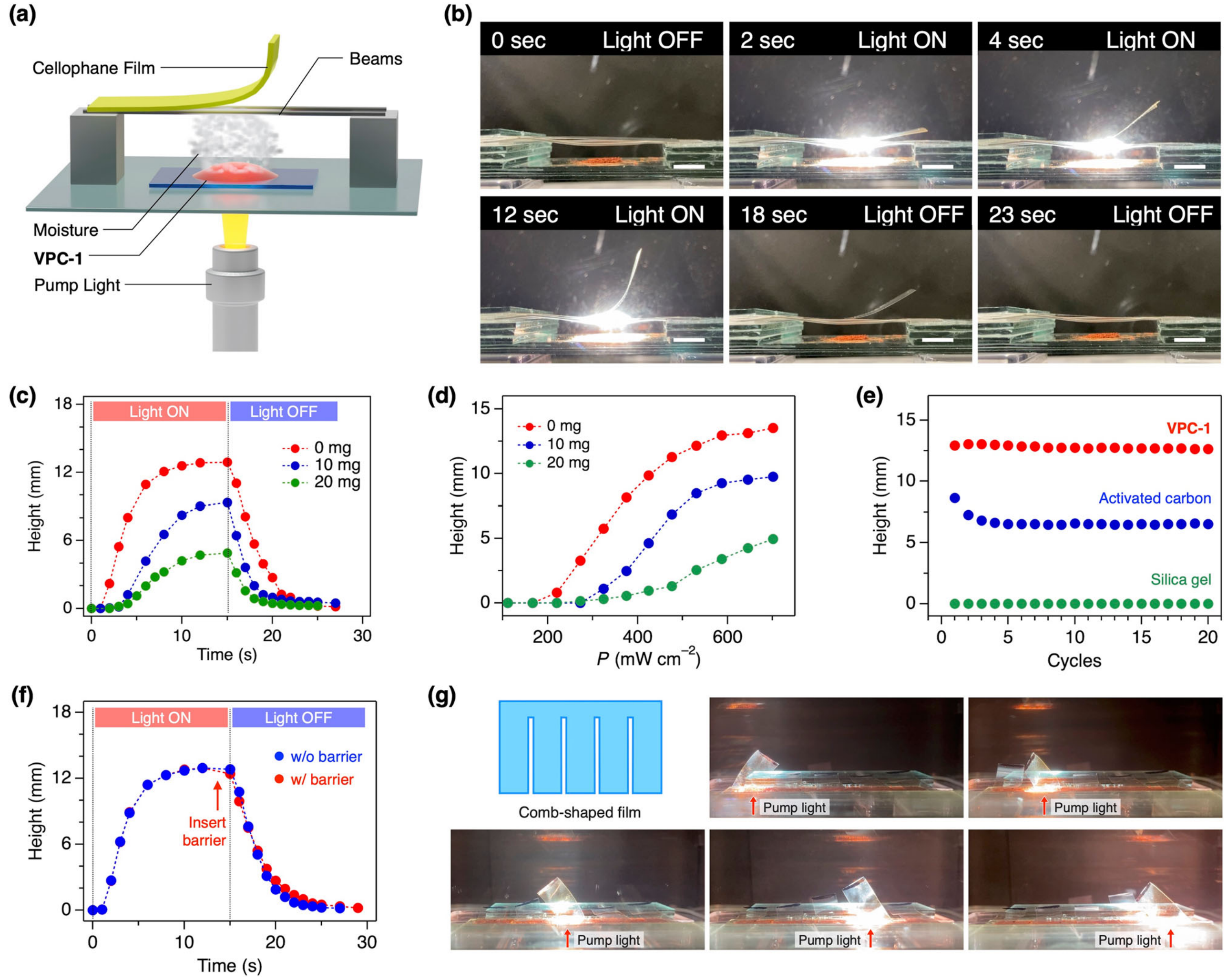

Fig. 4 | Film actuation with VPC-1. **a** Experimental setup for measuring the transformation of a cellophane film put above **VPC-1**. **b** Photographs of the cellophane film bent upward by the moisture from **VPC-1**. Scale bars: 5 mm. **c** Time-course change in the height of the film edge loaded with 0, 10, and 20 mg of silicone grease (red, blue, and green circles) upon irradiation with the pump light. **d** Plot of the bending height of the film loaded with 0, 10, and 20 mg of silicone grease (red, blue, and green circles) as a function of power density (*P*) of the pump light. **e** Changes of the bending height of the film when repeating the irradiation of pump light on **VPC-1**, activated carbon, and silica gel (red, blue, and green circles). **f** Time-course changes in the height of the film edge with and without the glass barrier (red and blue circles) inserted just before turning off the pump light as indicated by a red arrow. **g** Photographs of the comb-shaped film. The strips were individually actuated by spotting the pump light at different positions indicated by red arrows.

($\lambda = 500$ nm) with P of 80.2 mW cm^{-2} and desorbs 2.08 mmol of H_2O per 1 g of **VPC-1** at 60%RH according to the H_2O isotherm curves (Fig. S12) due to the decrease of the relative humidity to 29%RH at 35.0 °C. Half of the H_2O desorption completed in 13 sec according to Fig. 3b.

VPC-1 can release and adsorb water repeatedly by turning the pumping light on and off. We cast a pumping light with P of 72 mW cm^{-2} for 15 s with an interval of 15 s, at which the pump light was turned off. This cycle was repeated 30 times, and no obvious deterioration in the performance was observed (Fig. 3e). **VPC-1** reabsorbed water sufficiently just by lowering P below P_{th} rather than totally turning off the pumping light. When we oscillated P between 4.2 and 57 mW cm^{-2} repeatedly, **VPC-1** showed reversible color change (Fig. S21).

Actuation of a film with VPC-1. To demonstrate the utility of **VPC-1** as a light-responsive ultrafast humidifier, we put a thin film of cellophane above **VPC-1** and irradiated the pump light onto **VPC-1** from the bottom with an expectation that the moisture squeezed from **VPC-1** instantaneously increases the humidity at the bottom side of the film while keeping the humidity at the top side virtually constant, leading to the upward bending of the film (Fig. 4a). Upon shining the pump light at $t = 0$ s, the film bent upward with a bending angle up to 75° and a height of 12.9 mm (Fig. 4b, c). After turning off the light at $t = 15$ s, the bent cellophane eventually turned back to the initial shape in the following 15 s (Fig. 4c). The film stood still when conducting the same light exposure experiment without **VPC-1** or simply increasing the ambient humidity (Fig. S22). Thus, we concluded that the moisture provided from **VPC-1** was absorbed by the film and lead to the bending through the expansion of the bottom side of the film.

The force generated by the humidification was large enough to lift an object put on the cellophane film. As the weight, silicone grease was mounted on the edge of the film, and the displacement of the film edge was recorded with a camera (Fig. S23). When 0, 10, and 20 mg of silicon grease was loaded on the film, the film started to bend in 1, 3, and 5 s after the photoirradiation and halted the movement at height of 12.9, 9.3, 4.9 mm, respectively (Fig. 4d). We calculated the maximum lifting acceleration and force as 4.6×10^{-4} m s^{-2} and 9.1×10^{-9} N, respectively (Fig. S24). The power conversion efficiency from the pump light to the mechanical potential energy of the weight was 2.7×10^{-3}% (see Actuation experiments of cellophane films with **VPC-1** section in Methods for the details of the calculation).

As comparisons, we set activated carbon and dye-doped silica gel instead of **VPC-1** and conducted the same experiments. In comparison to the maximum H_2O uptake of **VPC-1** (6.3 wt%, 106.4 mL(STP) g^{-1}), both silica gel and activated carbon are known to feature larger H_2O uptake (20–65 and 16–40 wt%) according to literature[27–32], which we confirmed by ourselves using the pore & surface analyzer (Supplementary Data 9 and 12). The experimental values for silica gel and activated carbon used for the actuation experiments were 481.1, and 473.7 mL (STP) g^{-1}. However, the degree of the bending of the cellophane film was nearly negligible when using silica gel as a humidifier (Fig. 4e green circles and S25). Activated carbon, featuring high water adsorption capacity and photoabsorption efficiency[33–35], was capable of actuate the cellophane film, but the degree of the bending was ~50% of that achieved with **VPC-1** (Fig. 4e blue circles and S25). Moreover, the degree of bending became smaller as repeating the experiments, while **VPC-1** did not show any distinguishable change in performance (Fig. 4e red circles). The decline in the film actuation ability is likely attributed to the slower H_2O adsorption kinetics and associated incomplete H_2O uptake within the interval (45 sec) between each cycle. The actuation speed is also slower. To quantitatively evaluate the actuation speed, we define the time constant of actuation as the time required for the film to reach 50% of its maximum height. Activated carbon induces the bending with a time constant of 6.8 sec (Fig. S26), while that of **VPC-1** is 3.4 sec.

As a further demonstration of **VPC-1**, we tested the ability as a humidifier in an open condition. In contrast to the experiments in Fig. 4a, in which **VPC-1** and the film were enclosed in a container to make the experimental conditions constant, here, we put **VPC-1** and the cellophane film in the ambient atmosphere without any housing. Even in such an open condition, the film actuation was nearly identical to that observed in the container (Fig. S27).

We also investigated whether **VPC-1** was effective in the dehumidification. As described above, the recovery of the film to the initial straight shape was completed within 15 s after turning off the pumping light. Synchronous to the straightening, the colour of **VPC-1** went back to red rapidly, giving evidence of the re-adsorption of humidity from the atmosphere (Fig. S28). To elucidate the effect of the de-humidification by **VPC-1** on the film actuation, we inserted a glass plate (40 × 20 × 1.2 mm) between the film and **VPC-1** just before stopping the light irradiation so that the de-humidified atmosphere did not approach to the film (Fig. 4f). When the glass plate barrier was inserted, the recovery of the film shape was slightly delayed than that without the barrier, whose change was larger than the error bars (Fig. S29). This result indicates that **VPC-1** accelerates the backward motion of the film.

As the demonstration of the spatiotemporal and remote humidification with **VPC-1**, a comb-shaped cellophane film was prepared and was actuated like fingers (Fig. 4g). When irradiated with a pump light with *d* of 1 cm, each strip bent upward individually depending on the spot position.

Conclusions

In conclusion, we found that a van der Waals porous crystal **VPC-1** can retain porosity throughout the transformation of the crystal structure. The change in conformation and packing was unambiguously visualized by means of electron and X-ray diffractometry, showing the rotational motion of the peripheral units of the host molecule. The aromatic pore surface and the conformational change allowed the guest water molecules to be transported in the pores at a fast rate (490 μs) in response to visible or IR light irradiation. The humidification of the surrounding atmosphere with **VPC-1** was so intense and quick that a cellophane film, put above the powder of **VPC-1**, bent upward with the maximum acceleration and speed of 7.3×10^{-4} m s^{-2} and 1.5×10^{-3} m s^{-1}, respectively. The single-crystal structure revealed herein provides an insight into how the molecules can move within a porous crystal that is sustained by van der Waals interactions. This finding suggests a huge potential of porous crystals as a quick and intense humidifier that can be operated remotely. This finding also implies the potential functionalities achievable by mere stacking of discrete molecules. The molecular design and bonding chemistry of van der Waals porous crystals are totally distinct from those of the existing porous crystals and, therefore, will lead to an unprecedented outcome in the future.

Methods

Materials

Chemical reagents were purchased from FUJIFILM Wako Pure Chemical Corp. and used as received. The activated carbons were purchased from UES Co., Ltd. **G2DBPHZ** was synthesized and crystalized to form **VPC-1** according to our previous report[22].

Electron diffraction

VPC-1 powder was ground gently and transferred into a 1.5 mL glass vial. A lacey carbon grid was then placed directly into the vial. The vial was shaken, and the grid was transferred quickly into the sample holder of the electron diffractometer. Continuous rotation 3D electron diffraction data was acquired using the dedicated electron diffractometer Rigaku XtaLAB Synergy-ED, equipped with a HyPix-ED detector by Rigaku. Data acquisition was performed at ambient temperature with an electron wavelength of 0.0251 Å (200 kV). The data were processed using CrysAlis$^{\text{Pro}}$ for ED, the structure was solved using SHELXT and subsequently refined using SHELXL in the crystallographic program suite Olex2.

Rietveld structure analysis

The powdery specimens of **VPC-1** sealed in a glass capillary were exposed to synchrotron X-ray irradiation at the beamline BL5S2 of Aichi Synchrotron Radiation Center. Rigid-body Rietveld analysis was carried out for data using the program SP[36]. The molecular structure of the without water from ED was used for the initial model.

Diffuse reflectance analysis

Typically, a 2.0 mg powder of **VPC-1** is put on a glass plate and set in a steel chamber. The top side of the chamber is covered with a thin glass plate to allow the pumping and probing light to pass through. The chamber is equipped with an inlet and outlet tubes at both sides for flowing dry/humidified N_2 gas at a flow rate of 1 L min^{-1} with humidity varied from 0–95% RH. The pumping light for photothermal heating is generated from a Xenon lamp (Asahi Spectra Co., Ltd. model MAX-350), passes through a bandpass filter (bandwidth of 25 nm) with its central wavelength varied from 400 to 725 nm, and is cast onto **VPC-1** via an optical fiber. The incident angle of the pump light is orthogonal to the glass substrate, and the spot diameter (*d*) is 8 mm, which is nearly same with the area covered by **VPC-1** powder. A green semiconductor laser module (Thorlabs Inc. model CPS-532, $\lambda = 532$ nm, output power 4.5 mW, $d = 3.5$ mm) was used as the probe light. The probing light was directed diagonal ($\theta = 35°$) to the glass substrate. The scattering of the probe light was collected with an optical fiber (Thorlabs Inc. model M25L05, core diameter: 200 μm, NA 0.22) set diagonal to the substrate ($\theta = 35°$) and diagonal to the plane of incidence of the pump light ($\theta = 21°$), and 2 cm separated from the chamber. The collected light was transferred to a spectrometer (Teledyne Princeton instruments Inc. model HRS-300MS-NI-G3) through a bandpass filter ($\lambda = 532$ nm, full-width at half-maxima = 3 nm). The humidified gas was generated by bubbling N_2 gas through liquid water and was mixed with the pristine dry N_2 gas with a certain mixing ratio, which was tuned by using regulators (KOFLOC Corp. model RK1650).

Temperature measurement during visible light irradiation

Temperature measurements during the visible light irradiation were performed by embedding a type K thermocouple (ANBE SMT Co. model KMT-100-100-200, diameter of 200 μm) connected to a digital thermometer (Custom Corp. model CT-470) in the stack of a powdery specimen of **VPC-1** (Fig. S19), which was then investigated under the pump light and in the same humidity control chamber written above.

Diffuse reflectance measurements with the FEL irradiation

The IR laser pulse was generated from a mid-IR free electron laser (KU-FEL, Institute of Advanced Energy, Kyoto University)[26] with a pulse width of 3 μs, pulse energy of 0.80–4.2 mJ, spot size of 2 mm, and a repetition rate of 2 Hz. A wire grid polarizer (Thorlabs, Inc. model WP25H-K) inserted in the FEL beam path was used for adjusting the pulse energy. A semiconductor laser (Thorlabs, Inc. model CPS-532, $\lambda = 532$ nm, output power 4.5 mW) attenuated by a neutral density filter with an optical density of 2.0 (Thorlabs, Inc. model NDUV20A) was used as the probe light. The probe light was focused on the sample by a plano-convex lens (Thorlabs, Inc. model LA5255, focal length = 250 mm). The scattered probe light was detected with a photomultiplier tube (Hamamatsu Photonics K.K. model R1477). A neutral density filter (Thorlabs, Inc. model ND20A) was used to attenuate the intensity of the probe light injected into the photomultiplier tube. A bandpass filter (Thorlabs, Inc. model FL532-3, center wavelength of 532 nm, full-width at half-maximum of 3 nm) was used to selectively measure the reflected probe laser. **VPC-1** was put in a steel chamber with a BaF_2 glass ceiling to allow IR and probe light path thorough (Fig. S16). The temperature of the chamber is stabilized within ±0.05 K. The humidity of the flowing gas was regulated with a water vapor generator (Rigaku Co., Ltd. model HUM-1).

Adsorption rate measurements

The adsorption rate of water vapor in **VPC-1** was measured with a MicrotracBEL Corp. model Belsorp-Max. Temperature of the sample during adsorption measurements was fixed at 25 °C by circulating water. **VPC-1** was degassed at 50 °C for at least 24 h prior to the measurements. The adsorption rates were evaluated at 25 °C by monitoring the time-dependent change in pressure after the introduction of a fixed volume of H_2O vapor into the sample chamber, using the BELSORP MAX application.

Actuation experiments of cellophane films with VPC-1

A thin film of cellophane (width of 2 cm, length of 4 cm, and thickness of 30 μm) was set at 0.4 cm above 3.0 mg of **VPC-1**. One end of the film was fixed to a bank made of glass plates. The other end of the film was not fixed. Between the banks, two tin wires were bridged so that the film did not bend downward by the gravity force. The whole setup is placed in a transparent plastic container (28 × 19 × 14.5 cm), and the pump light with P of 730 mW cm^{-2} is directed from the bottom side of the container. The white light generated from the Xenon lamp is cast without using bandpass filters. The morphological change of the film is observed with a camera set horizontal to the film.

The power conversion efficiency η was calculated based on the equation below:

$$\eta = \frac{m \times g \times h}{P \times A \times t} \tag{1}$$

where m is the weight of the loaded silicone grease, g is the gravitational constant, h is the highest latitude of the lifted grease, P is the power density of the pump light, A is the spot size of the pump light, and t is irradiation time.

The comb-shaped cellophane film is prepared by cutting a film to have five strips, each of which has dimension of 10-mm width and 30-mm length and are connected together at one end. The film is set at 5 mm above **VPC-1** cast over an area of 10 mm × 70 mm.

DFT Calculations

All calculations (Supplementary Data 13) were performed at the framework of the DFT using the CAM-B3LYP[37] and ωB97XD[38] functionals together with the 6-31 G** basis set[39,40] as implemented in the Gaussian16[41] program.

In line with the experimental crystalline structures, three different theoretical models have been considered for the **G2DBPHZ** system in which the external Cz dihedral angles are kept fixed at 40° while the internal dihedral angles between the DBPHZ core and the adjacent internal Cz units vary from 70° in model 1 (as in the crystal obtained under atmosphere with a humidity of 92%RH) to 45° in model 3 (as in the crystal packing obtained under vacuum), passing through an intermediate point at 60° (model 2) taken to illustrate the influence exerted by the rotation (Fig. S6). The calculated frequencies were scaled by a factor of 0.95 to avoid experimental misassignments. Theoretical IR spectra were obtained by convolution of the scaled frequencies vs the IR activities with Gaussian functions (4 cm^{-1} width at the half-height). In this case, CAM-B3LYP functional is found to provide an improved quantitative agreement with the experimental IR data compared to ωB97XD functional.

To evaluate the conformational flexibility of the **G2DBPHZ** system, we have performed a rigid potential energy surface scan as a function of the inter-ring dihedral angle (θ) between the central DBPHZ spacer and the adjacent Cz unit, at the CAM-B3LYP/6-31 G** and ωB97XD/6-31 G** level of theory, respectively, obtaining very similar energy profiles.

For the calculations of aggregates, the ωB97XD functional, which includes an empirical dispersion correction term proposed by Grimme, was used due to its ability to accurately predict the π-π stacking interactions and the energies of the weak intermolecular interactions. The aggregation strength has been evaluated based on the interaction energies of the supramolecular aggregate (*i.e.*, dimer) with respect to its isolated molecular constituents, as indicated below: $\Delta E = E\text{dimer} - 2E\text{monomer}$.

Data availability

Additional Supplementary Figures, data, and tables supporting the findings in the main text are available in the Supplementary Information. All data relating to figures in the main text and Supplementary Information are available upon reasonable request from the authors. The single-crystal structure data reported in this article is deposited at the Cambridge Crystallographic Data Center (CCDC) under a deposition number of 2355950. The data can be obtained free of charge from The Cambridge Crystallographic Data Center via www.ccdc.cam.ac.uk/data_request/cif.

Received: 13 June 2024; Accepted: 14 November 2024;
Published online: 30 November 2024

References

1. Holst, J. R., Trewin, A. & Cooper, A. I. Porous organic molecules. *Nat. Chem.* **2**, 915–920 (2010).
2. Cooper, A. I. Molecular organic crystals: from barely porous to really porous. *Angew. Chem. Int. Ed.* **51**, 7892–7894 (2012).
3. McKeown, N. B. Nanoporous molecular crystals. *J. Mater. Chem.* **20**, 10588–10597 (2010).
4. Desiraju, G. R. Crystal engineering: a holistic view. *Angew. Chem. Int. Ed.* **46**, 8342–8356 (2007).
5. Yamagishi, H. Functions and fundamentals of porous molecular crystals sustained by labile bonds. *Chem. Commun.* **58**, 11887–11897 (2022).
6. Kitagawa, S., Kitaura, R. & Noro, S. Functional porous coordination polymers. *Angew. Chem. Int. Ed.* **43**, 2334–2375 (2004).
7. Yaghi, O. M., O'Keeffe, M., Ockwig, N. W., Chae, H. K., Eddaoudi, M. & Kim, J. Reticular synthesis and the design of new materials. *Nature* **423**, 705–714 (2003).
8. Waller, P. J., Gandara, F. & Yaghi, O. M. Chemistry of covalent organic frameworks. *Acc. Chem. Res.* **48**, 3053–3063 (2015).
9. Mastalerz, M. Permanent porous materials from discrete organic molecules-towards ultra-high surface areas. *Chem. Eur. J.* **18**, 10082–10091 (2012).
10. Horike, S., Shimomura, S. & Kitagawa, S. Soft porous crystals. *Nat. Chem.* **1**, 695–704 (2009).
11. Krause, S., Hosono, N. & Kitagawa, S. Chemistry of soft porous crystals: structural dynamics and gas adsorption properties. *Angew. Chem. Int. Ed.* **59**, 15325–15341 (2020).
12. Allcock, H. R. Cyclophosphazene clathrates - exploring adjustable tunnel. *Acc. Chem. Res.* **11**, 81–87 (1978).

13. Sozzani, P., Bracco, S., Comotti, A., Ferretti, L. & Simonutti, R. Methane and carbon dioxide storage in a porous van der Waals crystal. *Angew. Chem. Int. Ed.* **44**, 1816–1820 (2005).
14. Msayib, K. J. et al. Nitrogen and hydrogen adsorption by an organic microporous crystal. *Angew. Chem. Int. Ed.* **48**, 3273–3277 (2009).
15. Bezzu, C. G., Helliwell, M., Warren, J. E., Allan, D. R. & McKeown, N. B. Heme-like coordination chemistry within nanoporous molecular crystals. *Science* **327**, 1627–1630 (2010).
16. Bezzu, C. G. et al. Highly stable fullerene-based porous molecular crystals with open metal sites. *Nat. Mater.* **18**, 740–745 (2019).
17. Yamagishi, H. et al. Self-assembly of lattices with high structural complexity from a geometrically simple molecule. *Science* **361**, 1242–1246 (2018).
18. Reichenbächer, K. et al. Improved thermal stability of an organic zeolite by fluorination. *J. Incl. Phenom. Macrocycl. Chem.* **61**, 127–130 (2008).
19. Baroncini, M. et al. Photoinduced reversible switching of porosity in molecular crystals based on star-shaped azobenzene tetramers. *Nat. Chem.* **7**, 634–640 (2015).
20. McHale, C. M., Stegemoller, C. R., Hashim, M. I., Wang, X. & Miljanić, O. Š. Porosity and guest inclusion in cyclobenzoin esters. *Cryst. Growth Des.* **19**, 562–567 (2019).
21. Yamagishi, H. et al. Solvophobicity-directed assembly of microporous molecular crystals. *Commun. Chem.* **4**, 122 (2021).
22. Yamagishi, H. et al. Sigmoidally hydrochromic molecular porous crystal with rotatable dendrons. *Commun. Chem.* **3**, 118 (2020).
23. Qian, Q. et al. MOF-based membranes for gas separations. *Chem. Rev.* **120**, 8161–8266 (2020).
24. Krishna, R. Diffusion in porous crystalline materials. *Chem. Soc. Rev.* **41**, 3099–3118 (2012).
25. Sakata, Y. et al. Shape-memory nanopores induced in coordination frameworks by crystal downsizing. *Science* **339**, 193–196 (2013).
26. Zen, H., Suphakul, S., Kii, T., Masuda, K. & Ohgaki, H. Present status and perspectives of long wavelength free electron lasers at Kyoto University. *Phys. Procedia* **84**, 47–53 (2016).
27. Ascherl, L. et al. Solvatochromic covalent organic frameworks. *Nat. Commun.* **9**, 3802 (2018).
28. Foley, N. J., Thomas, K. M., Forshaw, P. L., Stanton, D. & Norman, P. R. Kinetics of water vapor adsorption on activated carbon. *Langmuir* **13**, 2083–2089 (1997).
29. Bedia, J., Rodriguez-Mirasol, J. & Cordero, T. Water vapour adsorption on lignin-based activated carbons. *J. Chem. Technol. Biotechnol.* **82**, 548–557 (2007).
30. Garg, A. et al. Gd(III) metal-organic framework as an effective humidity sensor and its hydrogen adsorption properties. *Chemosphere* **305**, 135467 (2022).
31. Chen, L. et al. Ultrafast water sensing and thermal imaging by a metal-organic framework with switchable luminescence. *Nat. Commun.* **8**, 15985 (2017).
32. Do, D. D. & Do, H. D. A model for water adsorption in activated carbon. *Carbon* **38**, 767–773 (2000).
33. Duan, R., Cui, G. M., Zhu, Q. Z. & Li, B. The radiation property of activated carbon particles in the visible to infrared spectrum. *Sol. Energy* **157**, 667–671 (2017).
34. Arshad, N. et al. Super hydrophilic activated carbon decorated nanopolymer foam for scalable, energy efficient photothermal steam generation, as an effective desalination system. *Nanomaterials* **10**, 2510 (2020).
35. Wang, P. Emerging investigator series: the rise of nano-enabled photothermal materials for water evaporation and clean water production by sunlight. *Environ. Sci. Nano* **5**, 1078–1089 (2018).
36. Nishibori, E. et al. Accurate structure factors and experimental charge densities from synchrotron X-ray powder diffraction data at SPring-8. *Acta Cryst. A* **63**, 43–52 (2007).
37. Yanai, T., Tew, D. P. & Handy, N. C. A new hybrid exchange–correlation functional using the Coulomb-attenuating method (CAM-B3LYP). *Chem. Phys. Lett.* **393**, 51–57 (2004).
38. Chai, J. D. & Head-Gordon, M. Long-range corrected hybrid density functionals with damped atom-atom dispersion corrections. *Phys. Chem. Chem. Phys.* **10**, 6615–6620 (2008).
39. Hehre, W. J., Ditchfield, R. & Pople, J. A. Self—consistent molecular orbital methods. XII. Further extensions of gaussian—type basis sets for use in molecular orbital studies of organic molecules. *J. Chem. Phys.* **56**, 2257–2261 (1972).
40. Francl, M. M. et al. Self-consistent molecular-orbital methods. XXIII. A polarization-type basis set for second-row elements. *J. Chem. Phys.* **77**, 3654–3665 (1982).
41. Frisch, M. J. et al. Gaussian 16 Rev. A.03, Wallingford, CT (2016).

Acknowledgements

This work was financially supported by Grant-in-Aid for Early-Career Scientists JP22K14656, Grant-in-Aid for Scientific Research(B) JP24K01306, Grant-in-Aid for Scientific Research(A) JP24H00470, Transformative Research Areas (A) JP24H01693 and JP23H03966, Scientific Research on Innovative Area "Aquatic Functional Materials: Creation of New Materials Science for Environment-Friendly and Active Functions" JP19H05716 and JP19H05717, from Japan Society for the Promotion of Science (JSPS), CREST (JPMJCR20T4) from Japan Science and Technology Agency (JST), the New Energy and Industrial Technology Development Organization (NEDO), Kato Memorial Bioscience Foundation, ZE Research Program, IAE (ZE2022B-19), Kyushu University Transdisciplinary Energy Research (Q-PIT), "ModuleResearch Program", "NJRC Mater. & Dev. (MEXT)", "Five-star Alliance" and the Cooperative Research Program. The work at the University of Málaga was funded by MICINN/AEI (project PID2022-139548NB-I00) and by Junta de Andalucía (P09FQM-4708 and P18-FR-4559). The authors would like to thank the computer resources, technical expertise, and assistance provided by the SCBI (Supercomputing and Bioinformatics) and the vibrational spectroscopy (EVI) lab of the Research Central Services (SCAI) of the University of Málaga. The powder X-ray diffraction experiments were conducted at the BL5S2 of Aichi Synchrotron Radiation Center (Proposal No. 202103069).

Author contributions

H.Y. and Y.Y. conceived the idea and designed the experiments. K.M. and H.Y. conducted the experiments. T.E., Y.T., S.M., E.H., and K.A. conducted the organic synthesis. H.Z. and Y.I. conducted experiments using the FEL. H.S. and E.N. performed the crystal structure analysis. I.B.D., J.S.R., and M.C.R.D. conducted the computational simulations. H.Y. and Y.Y. prepared the manuscript with feedback from the other authors.

Competing interests

The authors declare no competing interests.

Additional information

Supplementary information The online version contains supplementary material available at https://doi.org/10.1038/s42004-024-01366-1.

Correspondence and requests for materials should be addressed to Yohei Yamamoto or Hiroshi Yamagishi.

Peer review information *Communications Chemistry* thanks Katsumi Kaneko and the other, anonymous, reviewer(s) for their contribution to the peer review of this work. Peer review reports are available.

Reprints and permissions information is available at http://www.nature.com/reprints